Chapter 2

Slotted Fabry-Pérot Lasers

(to be updated as the chapter writing progresses)

As seen from Chapter 1, the need for low-cost tuneable lasers is increasing with the deployment of Fibre-to-the-x (FTTx) networks. This chapter presents the *Slotted Fabry-Pérot* technology as a solution to this need. The first section describes the theory behind the operation of slotted Fabry-Pérot lasers. The second section describes, in detail, the fabrication process for these type of lasers, which is low-cost and foundry compatible requiring no selective area bandgap engineering techniques. The third section presents experimental results obtained from these wavelength-agile lasers. And in the final section, a summary of the chapter is presented along with a discussion about the potential applications for slotted Fabry-Pérot lasers.

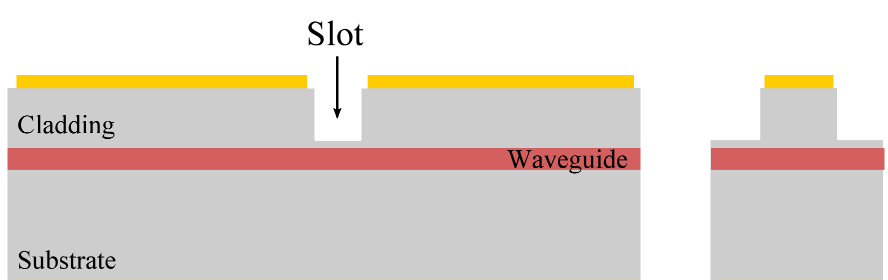

Figure 2.1: Schematic of a typical FP etalon based wavelength monitoring scheme used in commercial packages

The first mention of slots along the ridge waveguide of a laser in the literature was made in the 1980's by Coldren *et al*, who called it *grooves* in their paper [1]. Brian Corbett slots first time: . Describe how Coldren used it, and what kind of results they achieved, then describe how Corbett and we use it, and what are the differences [2]

2.1 Theory of Operation

2.1.1 Semiconductor Heterostructures

The first demonstration of coherent light emission from a semiconductor diode (based on Gallium Arsenide) was done by Hall *et al* [3] and Nathan *et al* [4] in 1962. These lasers and the other common designs of that era were homojunction lasers, i. e. the active core layer and the cladding were both made from the same material (GaAs) and thus had the same bandgap and refractive index. They had threshold current densities of about 1000 A/cm^2 at a low temperature of 77K, but at room temperature of 300K, the threshold current densities were orders of magnitude higher at about 100000 A/cm^2. This is mainly due to the fact that electrons and holes are free to diffuse, i.e. there is poor carrier confinement which results in poor gain. This meant that the lasers could operate at continuous wave (CW) mode only at low temperatures and could exhibit only pulsed mode operation at room temperature.

The concept of a heterojunction was introduced in 1954 by Kroemer [5] where two different semiconductor materials with varying bandgaps could be used. In a heterojunction, the bandgap of the p-type layer could be raised above that of the n-type layer underneath. This helps in creating a large potential barrier for minority carriers thus essentially only injecting the majority carriers from the wider bandgap material to the lower one. This achieves better optical confinement compared to homojunctions thus reducing the threshold current. In the mid 1960s, with the advance of epitaxial methods, in particular the possibility of liquid phase epitaxy of aluminium gallium arsenide, heterojunctions could now be created. Despite the increase in carrier confinement, the threshold current density could only be reduced around 10 times still making single-heterojunction lasers unable to exhibit CW lasing at room temperature [6].

The solution to achieving even better carrier confinement than a single heterojunction is to sandwich the active material on both sides with a higher bandgap material, which came to be known as a *double heterostructure* (DH) laser, as illustrated in Figure 2.2. This concept of a DH laser diode was first introduced by Kroemer [7] and Alferov *et al* [8] in 1963, and the fist semiconductor lasers to demonstrate CW operation at room temperature were indeed based on a double heterostructure in 1970 [9, 10]. Kroemer and Alferov went on to receive the Nobel prize for physics in the year 2000.

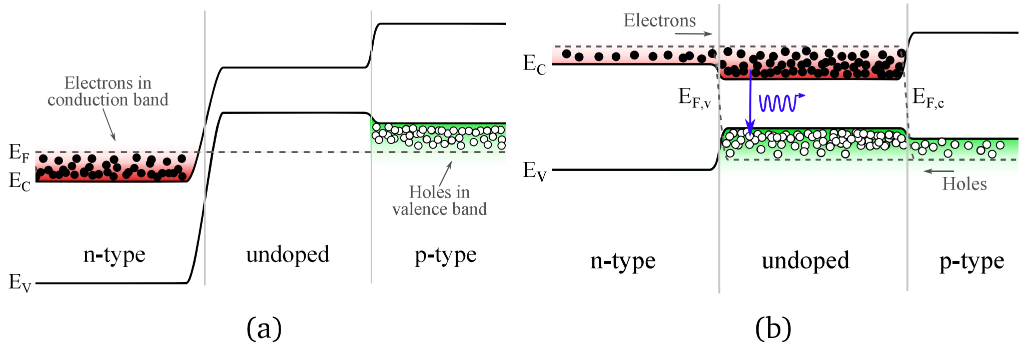

Figure 2.2: Illustrations (simplified) of band structure in a double heterostructure at (a) equilibrium - unbiased and (b) forward bias

When a double heterostructure is forward biased, electrons are injected into the active region from the n-type semiconductor and holes are injected into the active region from the p-type semiconductor. The higher bandgap on both sides ensures that electrons cannot escape into the p-type material and holes cannot escape into the n-type material. Thus electrons and holes are forced to recombine in the active region, leading to emission of photons. The carrier confinement can thus obtained in DH diodes for a bandgap difference of at least 0.25 eV between the active and the cladding regions [11].

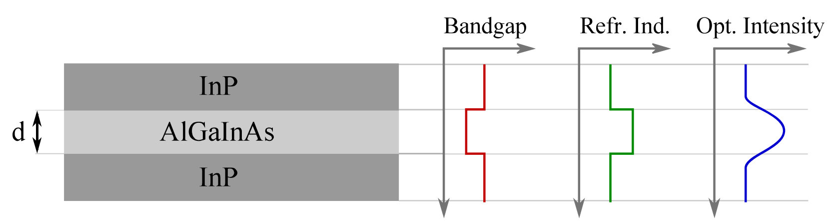

Figure 2.3: Illustration of the bandgap, refractive index and optical intensity profiles along a double heterostructure

Along with carrier confinement, another important requirement for an efficient laser diode is optical confinement. A convenient coincidence that can be exploited in this context is that the refractive index at a wavelength decreases with increase in bandgap. This means in a DH scenario, when a material with a lower bandgap is sandwiched by materials with higher bandgaps, the refractive index is highest in the middle layer and lower in the outer cladding layer on either side. The light that is generated in the active layer is confined well inside itself owing to the fact that an optical waveguide is formed in the transverse direction resulting from the refractive index profile as illustrated in Figure 2.3.

2.1.1.1 Semiconductor Material Systems

In order to choose the appropriate material system for the fabrication of the laser, we need to take into consideration a few key points. A semiconductor double heterostructure is grown using epitaxial methods needing high crystalline quality, which requires that the materials should be lattice matched perfectly. This requirement means that substrates could be binary III-V compound semiconductors like GaAs or InP since their lattice constants are defined unambiguously by stoichiometry. And depending on the substrate used, ternary or quaternary alloys can be used as the lower bandgap material. For example, AlGaAs can be lattice matched to GaAs and alloys like InGaAsP and AlInGaAs can be lattice-matched to an InP substrate.

It is also beneficial if the difference in bandgap energy between the two materials in the DH structure is as large as possible for better efficiency. In this context, quaternary alloys may have an edge as they have two parameters to vary compared to one in ternary alloys. For example, in $Al_xGa_yIn_{1-x-y}As$ the mole fractions of aluminium (x) and Gallium (y) can be varied, whereas in $Al_xGa_{1-x}As$ only the mole fraction of aluminium (x) can be varied. Having two variables lets us choose from different bandgap energies while simultaneously trying to satisfy the lattice matching requirement. In practice, the most widely used material systems for semiconductor lasers are AlGaAs on GaAs and InGaAsP/AlInGaAs on InP. Material systems involving GaAs substrates cover wavelength ranges below 900nm whereas the ones using InP substrates cover wavelengths over 1200nm. In this work, since we deal with wavelengths for telecommunication applications, which are around the 1550nm region, we choose a material system based on an InP substrate. Furthermore, AlInGaAs on InP was preferred over InGaAsP on InP because the conduction band offset is larger in the former ($\Delta E_c = 0.72\Delta E_g$ compared to $\Delta E_c = 0.40\Delta E_g$ in the latter) which leads to improved carrier confinement [12, 13].

2.1.2 Optical Waveguiding

2.1.2.1 Transverse Waveguiding

Using a double heterostructure as described above, an optical waveguide in the transverse direction can be formed. The optical modes supported by this waveguide can be *guided* or *radiation* modes. We shall concentrate on the guided modes, which can be further classified into *Transverse Electric* (TE) or *Transverse Magnetic* (TM) modes. In these modes only the electric field component (for TE) or the magnetic field component (for TM) lies in the plane perpendicular to the direction of propagation. Usually in semiconductor lasers, only TE modes are generated because they are more strongly guided in the waveguide and because the end facet reflectivity for TE modes is higher than that for TM.

It is useful to define a parameter known as the *optical confinement factor*, which is a measure of the optical power confined in the active region compared to the total optical power. Using the vertical direction in Figure 2.3 as the x-coordinate beginning from $-\infty$ at the bottom, passing through 0 at the lower interface between InP and AlGaInAs and increasing in the upwards direction, we can write the confinement factor, Γ as:

$$\Gamma = \frac{\displaystyle\int_0^d |E(x)|^2 \, dx}{\displaystyle\int_{-\infty}^{\infty} |E(x)|^2 \, dx} \tag{2.1}$$

Usually exact confinement factors are calculated numerically, but there exists a good approximation proposed by Botez [14], which is given by:

$$\Gamma \approx \frac{\Gamma'}{1+\Gamma'} \quad \text{where} \quad \Gamma' = 2\pi^2 \left(n_1^2 - n_2^2\right) \left(\frac{d}{\lambda}\right)^2 \tag{2.2}$$

where n_1 and n_2 are the refractive indices of the core and the cladding materials respectively, and λ is the wavelength. For a wavelength of 1550nm and a cladding material of InP (with n_2 = 3.167), the confinement factor is plotted in Figure 2.4 using Equation 2.2 for different values of n_2. In the devices presented in this thesis, the active region is AlInGaAs which has a refractive index contrast around 0.3 relative to InP, which corresponds to the red curve in Figure 2.4.

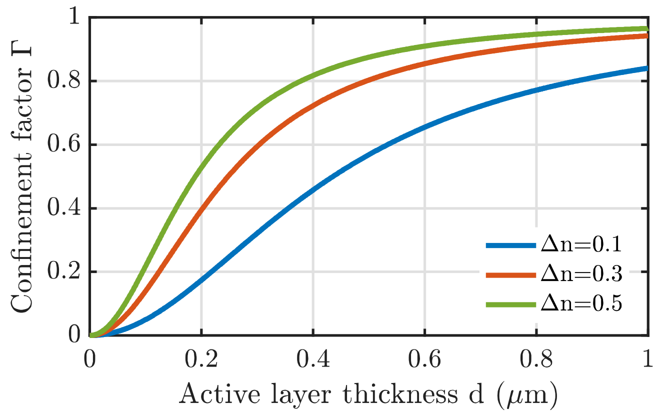

Figure 2.4: Confinement factor vs active layer thickness for different refractive index contrasts at 1550nm for an InP substrate

Generally, the epitaxial structure is designed such that only the fundamental mode is guided in the waveguide. The condition for this to occur is [11]:

$$d < \frac{\lambda}{2\sqrt{n_1^2 - n_2^2}} \tag{2.3}$$

In our case, this translates to an active layer of thickness less than 550 nm.

2.1.2.2 Lateral Waveguiding

In the previous section, we have discussed transverse waveguiding in the laser structure. However, for stable and well-defined laser operation, it is also necessary to have waveguiding in the lateral direction [11]. This can be achieved in two ways, known as *index guiding* (IG) and *gain guiding* (GG). In IG structures, a ridge-type geometry is fabricated in the lateral direction, thus forming a waveguide with the semiconductor as the core and air (in most cases) as the cladding layer. Along with the epitaxial structure in the transverse direction, this effectively forms a two dimen. On the other hand, in GG structures, there are no geometrical features in the lateral direction. The waveeguiding in the lateral direction is entirely based on confining the gain to a narrow region. This is achieved by a stripe metal contact where the injected current is restricted to a few microns.

The waveguiding in GG lasers is usually much weaker than in IG lasers. This causes many impairments such as beam instabilities, astigmatic fields, multimodal behaviour and higher threshold currents [11]. Hence for application in optical communication, index guided lasers are preferred which are also used in this thesis work.

2.1.3 Quantum-Well Laser Diodes

The first semiconductor DH laser materials were grown using liquid phase epitaxy (LPE). During the growth process, the wafer had to be quickly moved in the LPE machine between different melts of materials - the n-type, p-type and undoped material. This had to be done rapidly since the active region had to be less than a micron thick. With the advance in epitaxial techniques, especially molecular beam epitaxy (MBE) and metal organic vapour phase epitaxy (MOVPE) it was possible to control the epitaxial growth at almost atomic layer, capable of producing very thin layers, which are called *quantum well* (QW) structures [11]. If the thickness of the core layer is smaller than the de Broglie wavelength of the carriers (about 15nm) quantisation effects start to appear. The density of states is modified as illustrated in Figure 2.5, and this leads to an increase in the differential gain since the injected carriers are now spread over a narrower energy range due to the quantisation.

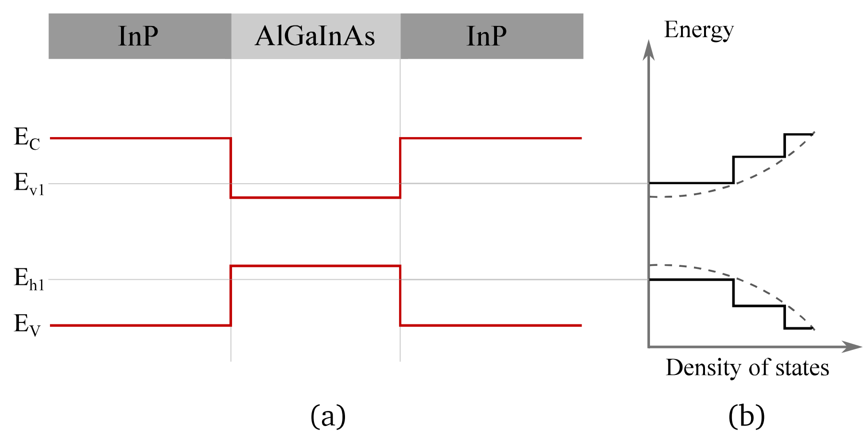

Figure 2.5: Illustration of the (a) conduction band and valence band edges and (b) the density of state in a quantum well (solid curve) and bulk semiconductor (dashed)

The requirement of lattice matching in quantum well structures can be more relaxed than bulk structures owing to the extreme small thickness of the grown layer. Hence, a small amount of strain, f, can be tolerated where f is given by:

$$f = \frac{a - a_0}{a_0} = \frac{\Delta a}{a_0} \tag{2.4}$$

where a_0 is the lattice constant of the substrate and a is the lattice constant of the layer grown on top of it. The critical thickness, h_c up to which the strained layer can be grown without damaging the entire crystal structure is given by [15]:

$$h_c = \frac{a}{32\sqrt{2}\pi f^2}\frac{1+\nu}{1-\nu}\ln\left(\frac{\sqrt{2}h_c}{a}\right) \quad (2.5)$$

where ν is the Poisson ratio, which is approximately 0.33 for most semiconductors [11]. Combining Equations 2.4 and 2.5 we can write:

$$h_c = \frac{a_0}{32\sqrt{2}\pi}\left(\frac{1+f}{f^2}\right)\frac{1+\nu}{1-\nu}\ln\left(\frac{\sqrt{2}h_c}{a_0(1+f)}\right) \quad (2.6)$$

Substituting the lattice constant a_0 = 0.587 nm of InP and ν = 0.33, we get:

$$h_c(nm) = 0.00206\frac{1+f}{f^2}\ln\left(\frac{2.4092h_c}{1+f}\right) \quad (2.7)$$

The analytic form of the above equation can be expressed as:

$$h_c(nm) = 0.4150(1+f)e^{-W_{-1}(-201.49f^2)}nm \quad (2.8)$$

where W_{-1} is the lower branch of the Lambert-W function. Equation 2.8 is plotted in Figure 2.6.

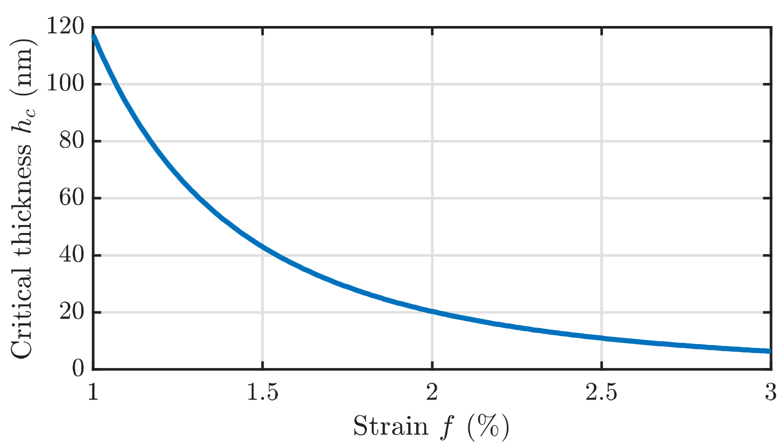

Figure 2.6: Critical thickness vs Strain for an indium phosphide substrate

We can see that strain values of around 2.5-3% can be tolerated by the core layer whose thickness is in the range of 10nm (as is required for the quantisation effects). Strained layers exhibit improved performance mainly due to the fact that the degeneracy of light and heavy hole valence bands is lifted by the strain. Hence, the density of states at the bottom of the valence band decreases resulting in population inversion for lower current densities [11, 16]. Thus, with the strain we have an additional degree of freedom for the design of the epitaxial layers and engineering the bandgap of the materials in order to achieve better efficiency. The devices presented in this thesis are fabricated on an epitaxial structure with a strain of about 1.2% in the quantum wells and a thickness of 6 nm, which is well under the critical thickness.

As we seen from the previous section on optical waveguides (Equation 2.2 and Figure 2.4)the optical confinement goes down as the active layer thickness decreases (for small values of the active layer thickness). Hence it is possible that the carrier confinement effects offered by the quantum wells are rendered useless due to poor optical confinement. We can see this illustrated in Figure 2.7 (a) which shows the carrier wavefunction along with the photon distribution. The optical confinement can be improved by adding an additional wave-guiding layer around the quantum well as shown in Figure 2.7 (b). This is usually known as *separate confinement heterostructure* quantum well (SCHQW) structures. Optical confinement and gain can be further increased by increasing the number of quantum wells - by the use of multiple quantum well (MQW) structures. The SCH structure can be made to have a constant composition (as in Figure 2.7 (b))or a graded composition, which leads to a graded refractive index. This is referred to as a GRIN (Graded Index) SCH QW structure. In a GRINSCH structure, the carrier confinement is achieved by the quantum well and the optical confinement is achieved by the surrounding waveguide structure, thus effectively decoupling the electronic and optical effects [17].

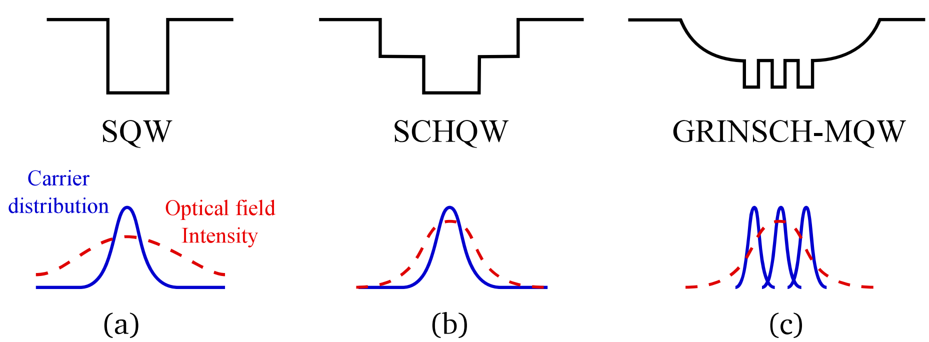

Figure 2.7: Illustration of carrier distribution and optical field intensity in (a) a single quantum well (b) an SCH-QW and (c) a GRINSCH-MQW

The substrates used for fabrication of the devices in this thesis are based on GRINSCH-MQW, i. e. a combination of a GRINSCH structure along with multiple quantum wells, which is schematically shown in Figure 2.7 (c). The refractive index of the material, which is inversely proportional to the bandgap energy, is shown in Figure 2.8 for the epitaxial layer structure used in this thesis.

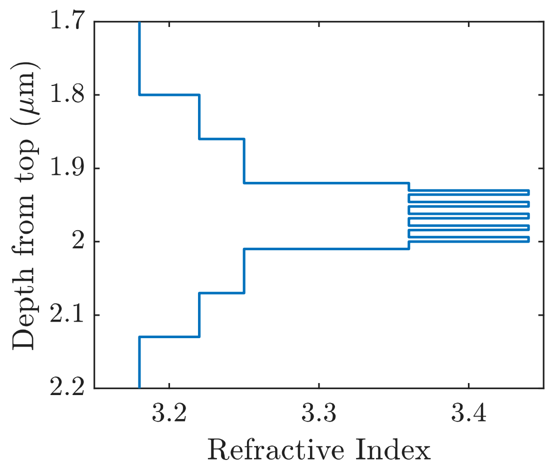

Figure 2.8: Refractive index profile of the epitaxial layer structure used in this thesis work To be changed to GRIN and maybe the axes flipped?

2.1.4 Waveguide Slot

In the previous sections techniques for optical waveguiding in the lateral and transverse directions have been introduced. To complete the design of a laser, we need a resonator in the longitudinal direction which is the third geometrical dimension. The ridge waveguide used for lateral confinement can be demarcated at the two ends forming a Fabry-Pérot (FP) cavity. Most laser diodes are based on a FP cavities, which are well documented in literature. The resonance condition for an FP cavity of length L is that the phase change after a complete round trip must be an integer multiple of 2π. This leads to a set of longitudinal lasing modes with wavelengths defined by:

$$\lambda_N = \frac{2n_{\text{eff}}L}{N} \tag{2.9}$$

where N in the mode number and n_{eff} is the effective refractive index. Usually for edge-emitting lasers, the dimension of the laser cavity is much larger than the operating optical wavelength. This leads to a large number of longitudinal modes. Hence under this approximation ($N \gg 1$), we can define a constant mode spacing given by [11]:

$$\begin{aligned} \Delta\lambda_m &= \lambda_N - \lambda_{N+1} \approx \frac{\lambda_N^2}{2n_{\text{g,eff}}L} \\ \text{where} \quad n_{\text{g,eff}} &= n_{\text{eff}}(\lambda_N) - \lambda_N \left.\frac{dn_{\text{eff}}}{d\lambda}\right|_{\lambda=\lambda_N} \end{aligned} \tag{2.10}$$

where $n_{\text{g,eff}}$ is the effective group index. Typically in an FP laser, these longitudinal modes are enveloped by the gain curve of the active medium. The width of this curve for AlInGaAs/InP material is several tens of nanometres. As illustrated in Figure 2.9, this leads to multiple longitudinal modes.

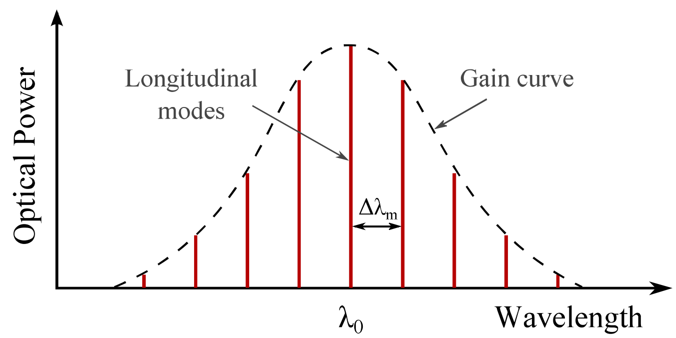

Figure 2.9: Longitudinal modes in a Fabry-Pérot laser

For applications in communication, we require lasers with a single wavelength output which translates to a single longitudinal mode. In order to achieve this we must make the gain curve sufficiently narrow so that only one mode is selected and the rest are filtered out. This *mode selection* can be done using various methods. As seen from Chapter 1, periodic structures such a Bragg gratings are used as mode selectors in single-mode laser designs such as the Distributed Bragg Reflector (DBR) and Distributed Feedback (DFB) lasers. In this work, we use *slots* along the Fabry-Pérot waveguide.

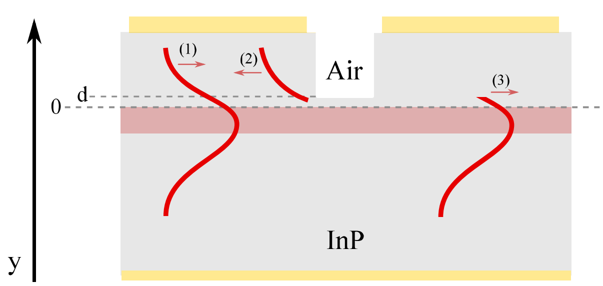

Figure 2.10: Illustration of reflection and transmission at a slot along the waveguide

Figure 2.10 provides an illustration of a slot etched into the ridge waveguide, which makes it a *Slotted Fabry-Pérot (SFP) Laser*. These slots provide reflections within the cavity which are wavelength dependent and thus aid in mode-selection to achieve single longitudinal mode lasing. In order to better understand the working of an SFP laser, we must first look at the reflections that arise from a slot. Figure 2.11 (a) and (b) show the optical field intensity inside a ridge waveguide simulated using a commercial mode solver (FIMMWAVE). We can observe that the intensity is a symmetric Gaussian-shaped beam around the quantum well region. This is schematically shown in Figure 2.10 marked as (1). At a slot, part of this field is reflected at the InP/air interface (marked as (2) in Figure 2.10) with a reflectivity value dictated by the refractive index difference between InP and air. The truncated field propagates forward as shown marked as (3) in Figure 2.10. This is justified from the numerical simulations of the optical field intensity at the slot, shown in Figure 2.11 (c) and (d), where we observe that the mode is pushed further into the substrate and is truncated rapidly going above the InP/air interface at the bottom of the slot.

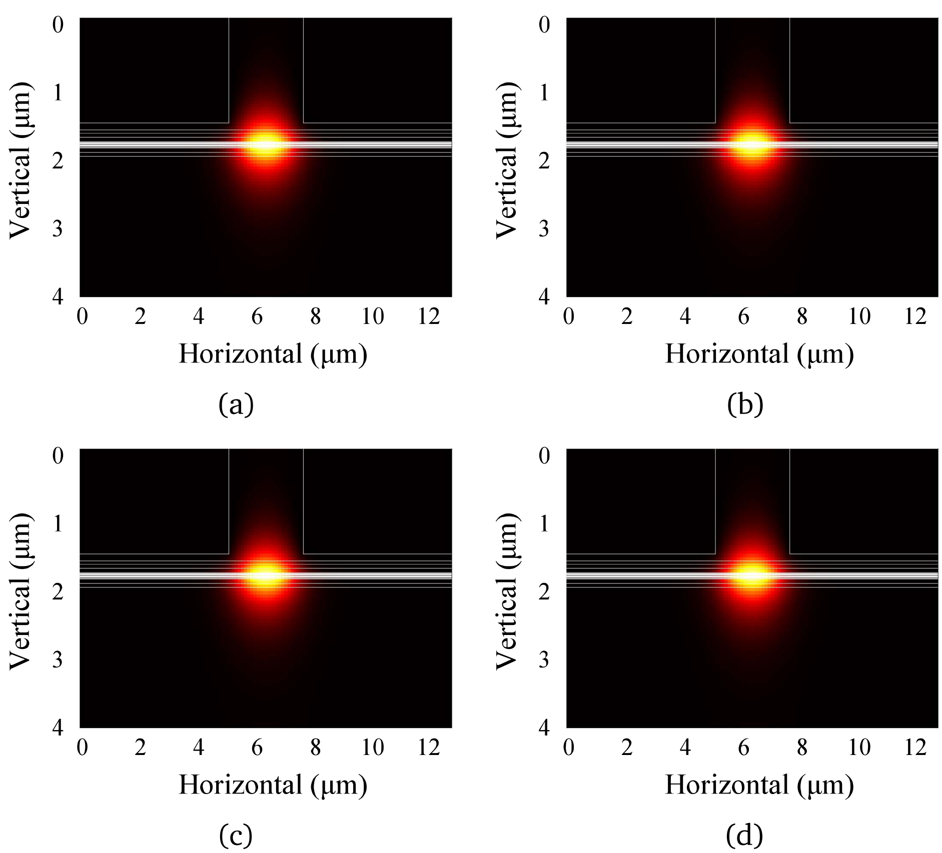

Figure 2.11: Change diagrams to illustrate slot model approximation

To calculate the reflectance of a slot r_s, we compute the overlap integral of the fundamental mode of the waveguide and the reflected field, given by [1]:

$$r_s = r\frac{\int_{-\infty}^{\infty} \Psi_r(y)\Psi^*(y)dy}{\int_{-\infty}^{\infty} \Psi(y)\Psi^*(y)dy} \tag{2.11}$$

and the transmittance, t_s, of a slot is given by:

$$t_s = \frac{\int_{-\infty}^{\infty} \Psi_t(y)\Psi^*(y)dy}{\int_{-\infty}^{\infty} \Psi(y)\Psi^*(y)dy} \tag{2.12}$$

where r is the bulk reflectivity at the air/InP interface given by

$$r = \frac{n_{\text{InP}} - 1}{n_{\text{InP}} + 1} \tag{2.13}$$

and $\Psi(y)$ is the fundamental mode field which corresponds to the curve in Figure 2.11 (b), and $\Psi_r(y)$ and $\Psi_t(y)$ are the reflected and transmitted optical fields respectively, which are given by (in the truncation approximation):

$$\Psi_r(y) = \begin{cases} \Psi(y) & ;\ y \geq d \\ 0 & ;\ y < d \end{cases} \tag{2.14}$$

$$\Psi_t(y) = \begin{cases} 0 & ;\ y \geq d \\ \Psi(y) & ;\ y < d \end{cases} \tag{2.15}$$

where d is the remaining thickness above the active layer after etching the slot. We assume that the remaining optical field which is neither reflected nor transmitted through at the slot, is lost into air at the InP/air interface. This loss incurred at the slot can be written as:

$$\eta_s = 1 - r_s^2 - t_s^2 \tag{2.16}$$

Using the above equations and the fundamental mode field given by Figure 2.11 (b), we can calculate the reflectance and transmittance of the slots as a function of the remaining cladding thickness above the slot, d, which are plotted in Figure 2.12.

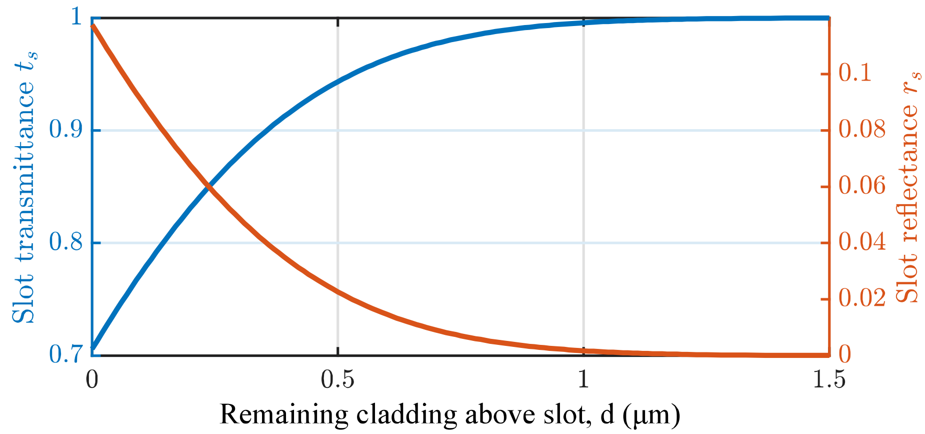

Figure 2.12: Reflectance and transmittance of a slot vs etch depth

From these calculations, the highest value of the achievable slot reflectance is observed to be around 0.118, which corresponds to a transmittance value of 0.706. From Equation 2.16, we can infer that the loss in this case is 48.8%. It is important to note from this discussion that loss due to the slot is directly proportional to the slot depth whereas the reflectance of the slot is inversely proportional to the slot depth. For effective single mode selection, we need high reflectance at the slot, but at the same time we also require low loss to achieve high optical output power. Hence, there is a trade-off between the single-mode behaviour and output power while choosing the etch depth of the slot. Another important aspect to be noticed is for low values of d, the slot reflectance is highly sensitive to any change in the value of d, or in other words, the any variation in the etch depth of the slot can cause a change in the mode-selection ant thus the output wavelength of the laser. This limits the repeatability of the tuning characteristics for such SFP lasers during different fabrication runs for the same design, where small changes in slot etch depths can result in quite different tuning maps.

2.1.5 Modelling Slotted Lasers

Etching a reflective slot into the waveguide essentially creates sub-cavities in the optical resonator which are coupled by the underlying active region waveguide. This creates a coupled-cavity effect which is well-known in literature [18, 19]. There exist various methods to model SFP lasers based on the coupled-cavity effect. When the slots were first proposed by Coldren *et al* [1], the truncation approximation described in the previous section was used. As single-mode lasers became more widely-studied in the following decades, there was a need to model them more accurately. The first of these methods was based on one-dimensional transmission matrices [20]. This method could not estimate scattering losses and also could not match the reflection coefficient with experimental measurements [21]. An improved two-dimensional scattering matrix method was proposed later [22] which could take into account the propagation and the transverse directions simultaneously. Yet another approach to modelling SFP lasers is the Time Domain Travelling Wave (TDTW) model [23]. In this approach the time-domain coupled-wave equations are solved at many discrete points along the length of the laser cavity as illustrated in Figure 2.13.

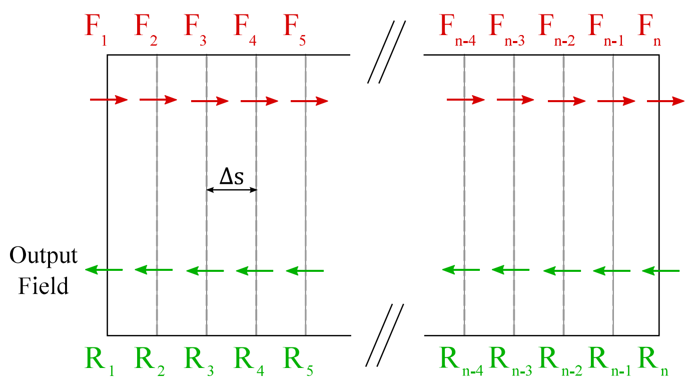

Figure 2.13: Discretisation used for the TDTW model

The forward and backward travelling fields are represented by $F(z,t)$ and $R(z,t)$ respectively, which can be written as:

$$\begin{aligned} \frac{1}{v_g}\frac{\partial F(z,t)}{\partial t} + \frac{\partial F(z,t)}{\partial z} &= (\Gamma g - \alpha - j\Delta\delta)F(z,t) + S_F(z,t) \\ \frac{1}{v_g}\frac{\partial R(z,t)}{\partial t} - \frac{\partial R(z,t)}{\partial z} &= (\Gamma g - \alpha - j\Delta\delta)R(z,t) + S_R(z,t) \end{aligned} \tag{2.17}$$

where v_g is the group velocity in the material, Γ is the optical confinement factor, g is the optical gain, α is the propagation loss in the waveguide and $\Delta\delta$ is the detuning factor. S_F and S_R are the spontaneous emission noise present in the waveguide in the forward and backward directions respectively, which is Gaussian-distributed. The time-dependent carrier rate equation is give by:

$$\frac{dN}{dt} = \frac{I}{eV} - \frac{N}{\tau} - BN^2 - CN^3 - 2v_g g\left(|F|^2 + |R|^2\right) \tag{2.18}$$

where I is the injected current, N is the carrier density, τ is the carrier lifetime,

V is the active region volume and B and C are the bimolecular and Auger recombination coefficients respectively. The optical gain g is given by:

$$g = \frac{g_N(N - N_0)}{2\left[1 + \epsilon\left(|F|^2 + |R|^2\right)\right]} \tag{2.19}$$

where g_N is the differential gain, N_0 is the transparency carrier density and ϵ is the nonlinear gain coefficient. The boundary conditions at the slot/air interface are given by the following:

$$\begin{aligned} F_m &= t_f F_{m-1} - r_f R_{m-1} \\ R_m &= t_f R_{m+1} - r_f F_{m+1} \end{aligned} \tag{2.20}$$

where t_f and r_f are the transmittivity and reflecitivity of a slot respectively, and the subscripts denote the m^{th} and $m + 1^{th}$ section at a slot as illustrated in Figure 2.14.

Figure 2.14: Reflection and transmission at a slot

Running the simulations using Equations 2.17, 2.18, 2.19 and 2.20, results from MATLAB simulation model

Show simulations showing gain is not clamped in a slotted laser compared to gain clamping in standard FP lasers

Show example lasing spectra from simulation

2.2 Etched Facets

The two important components of laser diodes are a material that provides optical gain and a mechanism for optical feedback. Typically for edge-emitting lasers the optical feedback is provided by cleaving the ends of the waveguide along the crystalline plane of the semiconductor material which results like mirror-like edges. And furthermore, after cleaving, thin-film coatings can be deposited on the facets to improve the reflectivity for greater optical feedback. Since the mirrors are essential to the working of the laser devices, this results in them not being testable on the wafer until they have been cleaved out and the coatings have been deposited. The handling of these fragile cleaved bars and testing them can lead to a significant incurred cost during mass production of such cleaved facet lasers.

An alternative to cleaved facet lasers is the *etched facet* approach. Here the mirrors are formed not by cleaving but by etching vertical facets at the end of the laser waveguides. There are numerous advantages to etched facets over cleaved facets. Since the facets are lithographically defined, the lengths of the waveguides can be controlled precisely. This eliminates errors due to mechanical cleaving of the facets. Furthermore, anti-reflection (AR) or high-reflection (HR) coatings can be deposited on the wafer instead of thin bars as is the case with the cleaved facet devices. Also, a deep facet etch exposes the underlying n-doped substrate which can be used to make n-contacts on the top side of the devices, along with the p-contacts. Having p and n contacts on the same side reduces complexity associated with wire-bonding and packaging of the device, especially for high-speed applications. Finally, as described earlier etched facets enable testing at the wafer level before dicing the devices which brings down the cost substantially [24].

In this work, etched facets not only form the end mirrors of the laser but also the separation between the laser section and the other active sections in the device such as the wavelength monitor and modulator. Although for a laser one would like to maximise the reflectivity of the facets, there could be cases where a low reflectivity is desired - such as in a Semiconductor Optical Amplifier (SOA). This can be achieved by etching the facets tilted at an angle to the waveguide and thus reduce optical feedback avoiding the creation of a resonant cavity. This is further explained in the following chapters.

2.3 Device Fabrication

2.3.1 Epitaxial Structure

The results presented in the following sections of this chapter are based on a device fabricated on a commercially available off-the-self wafer from the company IQE. Figure 2.15 shows a schematic of the epitaxial structure. The material is based on an indium phosphide (InP) substrate and is designed to have light emission at 1.55 μm. The epitaxial structure contains 5 compressively strained AlInGaAs quantum wells. The upper cladding is p-doped with Zinc and is around 1.6 μm thick, with an InGaAs layer on top to facilitate good metallic contact on the p-side. The structure incorporates a thin InGaAsP layer just above the active layer which is used as an etch-stop layer while etching the ridge waveguide geometry on the structure. This is further explained in the following section along with the other process steps. The substrate is about 400 μm thick and is n-doped using silicon. Optical confinement in the vertical direction is achieved by having the active region (higher refractive index) surrounded by the upper cladding and lower substrate materials with lower refractive index. The light is confined in the lateral direction using a ridge waveguide structure. The injection current is also delivered in a confined way through the use of the ridge waveguide. Table 2.1 summarises the epitaxial structure of the wafer and more comprehensive description of these layers in the epitaxial structure can be found in Appendix.

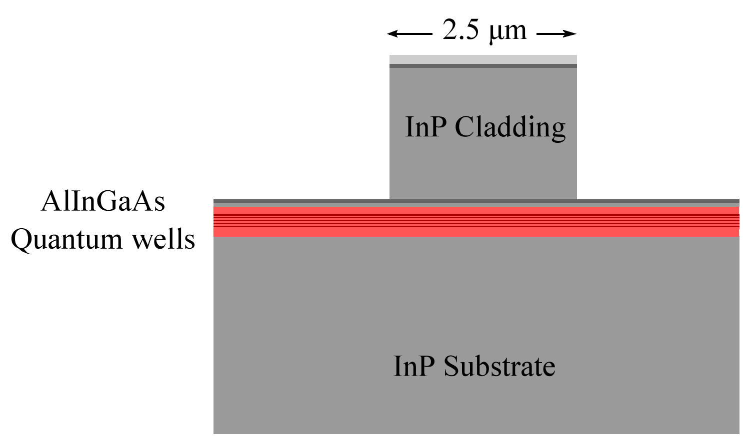

Figure 2.15: Schematic cross-section of the ridge waveguide showing the epitaxial layer structure

The entire epitaxial growth is performed commercially before the device processing which was done in-house as part of this thesis work. The process flow does not involve any epitaxial re-growth, which is common to conventional tuneable laser technologies. The absence of regrowth allows the use of AlInGaAs quantum wells which have higher conduction band offset compared to InGaAsP, which leads to higher optical gain and weaker temperature dependence [25, 26]. The aluminium content would otherwise make epitaxial re-growth challenging.

Table 2.1: Epitaxial structure of laser material from IQE

Material	x	y	Thickness (μm)	Dopant
GaIn(x)As	0.53		0.2	Zinc
GaIn(x)As(y)P	0.71	0.62	0.05	Zinc
InP			1.6	Zinc
GaIn(x)As(y)P	0.85	0.33	0.02	Zinc
InP			0.05	Zinc
[Al(x)Ga]In(y)As	0.90	0.53	0.06	Zinc
[Al(x)Ga]In(y)As	0.90-0.72	0.53	0.06	Undoped
[Al(x)Ga]In(y)As	0.44	0.49	0.01	Undoped
[Al(x)Ga]In(y)As	0.24	0.71	0.006	Undoped
[Al(x)Ga]In(y)As	0.44	0.49	0.01	Undoped
[Al(x)Ga]In(y)As	0.72-0.90	0.53	0.06	Undoped
[Al(x)Ga]In(y)As	0.90	0.53	0.06	Silicon
[Al(x)Ga]In(y)As	0.90-0.86	0.53	0.01	Silicon
InP			$\sim$ 400	Silicon

2.3.2 Processing Flow

The fabrication of the lasers is done on quartered pieces of a 2-inch wafer with the epitaxial structure described above. The six main steps are described briefly below. A comprehensive description of the processing flow along with the exact parameters can be found in Apppendix.

1. p-Metal Depostion

In this step, the p-contact metal on top of the ridge waveguide is deposited. This is done as the first step to help minimise the contact resistance between the p-metal and the semiconductor. A liftoff resist is spin-coated on to the wafer, above which a photoresist is spun on. A contact lithography is then performed on the photoresist using a mask aligner with UV-illumination. The photoresist is developed after the exposure, leaving the liftoff resist underneath exposed at the places where we desire the metal to be deposited. The liftoff resist is then developed using its own developer solution until it leaves a discernible undercut. 10nm of Titainum and 110nm of Gold is deposited on the whole wafer using a thermal evaporator. Finally the resists are stripped off using a photoresist-remover solution. This is schematically illustrated in Figure 2.16.

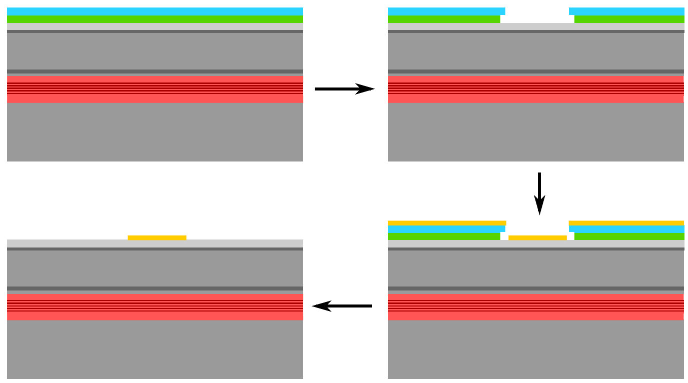

Figure 2.16: Liftoff process for p-metal deposition

2. Ridge Definition

A layer of silicon dioxide (SiO_2) is deposited over the whole wafer by the means of plasma enhanced chemical vapour deposition (PECVD). Photoresist is now spin-coated on top of the SiO_2 layer and patterned using photolithography, leaving the resist on places corresponding to the top of the ridge waveguide. Using the remaining photoresist as the mask, the SiO_2 is etched away using CF_4 and CHF_3 gases in an inductively couple plasma (ICP) etching process. Next, the photoresist is completely stripped off. We are now left with a SiO_2 hard mask protecting the top of the desired ridge waveguide. Next, the waveguide etch is etched using a mixture of Cl_2, H_2 and CH_4 gases in an ICP etcher. The etching rate of this chemistry for the semiconductor epitaxial layers is about 10 times faster than for the SiO_2 mask. This dry etch defines the ridge waveguide along with the reflective slots needed for wavelength control. We etch down to around 1.6 - 1.7 μm. This should leave us in the InP layer just above the InGaAsP layer in the epitaxial structure (Table 2.1). As seen from the previous section, the depth of this etch is crucial is determining the reflectivity of the slots. In order to achieve the exact desired depth, a wet etch is carried out using a solution of phosphoric acid and hydrochloric acid (1:4 H_3PO_4:HCl). The solution selectively etches InP but not InGaAsP. Thus, we can make sure that the final depth of the ridge exactly matches up to the InGaAsP layer 1.85 μm below the top of the wafer, i.e. just above the active layer to ensure maximum slot reflectivity, but no additional optical loss. Finally, the SiO_2 hard mask is etched away using the same CF_4 and CHF_3 ICP etch as described earlier. The entire process of ridge definition is schematically illustrated in Figure 2.17.

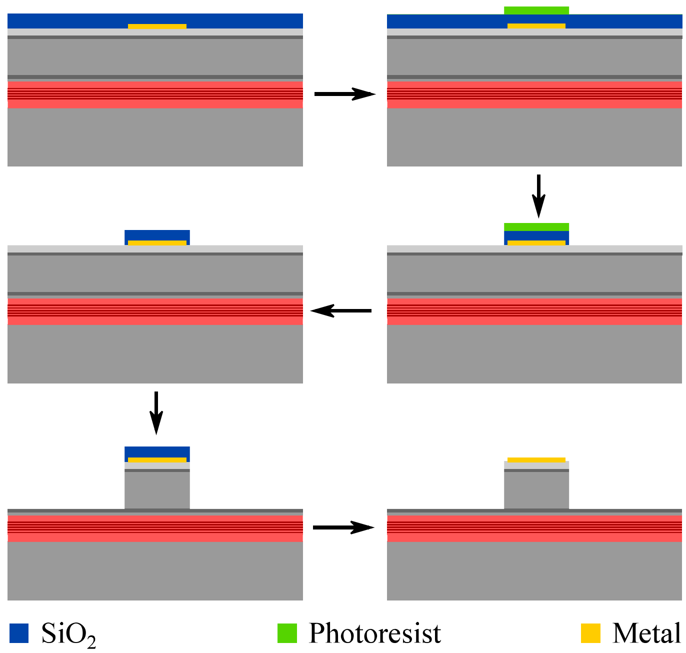

Figure 2.17: Ridge definition using an ICP etch

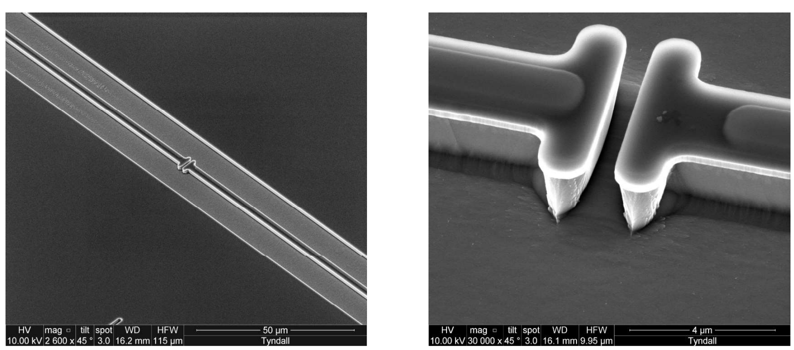

Figure 2.18: SEM images of the ridge waveguide and a slot

3. Facet Definition

Some lasers on the chip have one or both of their end mirrors using etched rather than cleaved facets. One of the reasons for having the rear mirror as an etched facet is the possibility to incorporate an integrated wavelength monitor behind the tuneable laser. The wavelength monitor is discussed in detail in the following chapter. Defining the etched facets follows a similar procedure as the ridge definition described in the previous step. A layer of SiO_2 is deposited using PECVD. A photoresist mask is then created, which helps in patterning the SiO_2 layer underneath. After the desired hard mask is created on the SiO_2 layer using a CF_4/CHF_3 ICP etch and the photoresist is stripped off, the semiconductor is etched using a Cl_2, H_2 and CH_4 ICP etch until a depth of about 5 μm. Finally, the SiO_2 hard mask is etched away. The entire process of facet definition is schematically illustrated in Figure 2.19.

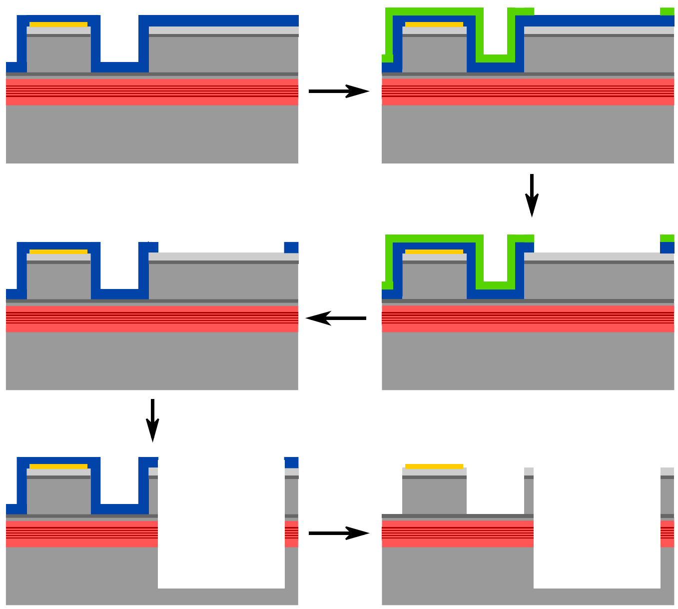

Figure 2.19: Facet definition using an ICP etch

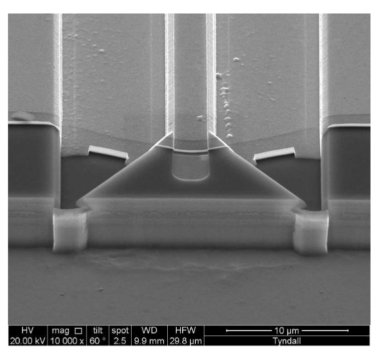

Figure 2.20: SEM image of an etched facet

4. Oxide Opening

To protect the sidewalls of the ridge waveguide, the entire structure is coated with a layer of SiO_2 using PECVD. This ends up covering the top of the ridge as well which has the p-metal contact. The metal needs to be exposed and available for probing in order to send in drive currents to the laser. In order to achieve this, the SiO_2 needs to be removed from the top of the waveguide. This is done by patterning a photoresist mask by photolithography, using which the SiO_2 is etched away using a CF_4/CHF_3 ICP etch. Since this ICP etch can damage the metal contact underneath the SiO_2, care is taken such that the ICP etch is stopped with a few nanometres of SiO_2 still remaining above the metal, which will be removed in the next step before depositing the p-metal contact pads. This process of oxide opening is schematically illustrated in Figure 2.21.

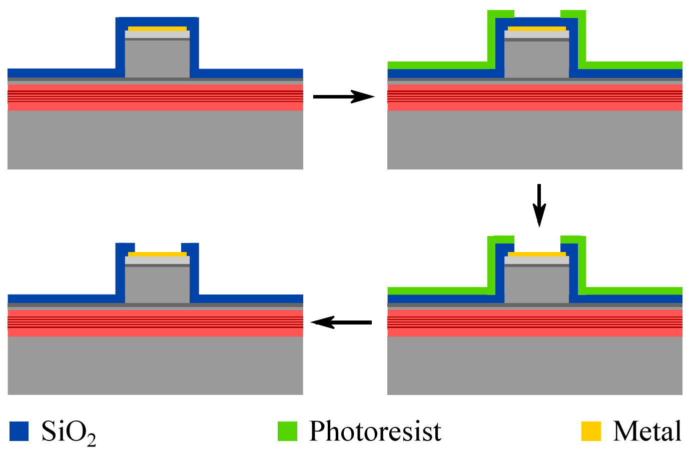

Figure 2.21: Liftoff process for p-metal deposition

5. p-Contact Pads Depostion

In this step, metal contact pads are deposited which connect to the top of the waveguide. In theory, the existing p-metal on top of the ridge can be probed to send in drive currents for the laser. But since physically probing the ridge is an extremely delicate process with a high probability of damage to the waveguide, it is better to have larger contact pads away from the ridge waveguide. This is done using a liftoff process similar to the first step in the fabrication process. A liftoff resist and a photoresist are spin-coated on the wafer and patterned. The liftoff resist is developed a little longer to leave an undercut beneath the photoresist. 10nm of Titanium and 340nm of Gold is deposited in a thermal evaporator using an angled and rotating holder, so that the metal can run along the sidewalls from the top to the bottom of the ridge. This process is schematically illustrated in Figure 2.22.

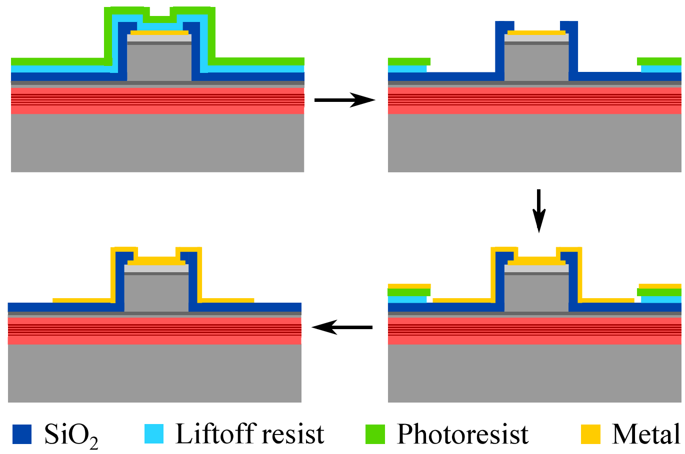

Figure 2.22: Liftoff process for p-metal contact pad deposition

6. Substrate Thinning and n-Metal Deposition

The next step of the fabrication process is to reduce the thickness of the substrate from around 400 μm to approximately 120 μm. This is essential to ensure good quality cleaving of individual devices as a thicker substrate can make the wafer hard to cleave. In order to achieve this, the wafer is first glued on to a glass carrier using black wax with its substrate facing upwards. The substrate is then treated to a Chemical Mechanical Polishing (CMP) process to get rid of its roughness using a commercially available sodium hypochlorite based polishing liquid (Logitech Chemlox). Next, the substrate is thinned using a solution of bromine and methanol (Br_2 / CH_3OH) to the desired thickness of 120 μm. Next, the n-metal, which is a combination of gold, germanium and nickel (Au:Ge:Au:Ni:Au 14:14:14:10:150nm) is deposited on to the substrate using a thermal evaporator. Finally the devices are cleaved out for further testing.

2.4 Experimental results

2.4.1 Effect of slots

To determine the effect of slot width and the number of slots on the optical characteristics, slotted Fabry-Perot laser devices were fabricated using the process described above with slot widths ranging from 0.8μm to 2μm with zero slots to 8 slots equally spaced along a given length of the Fabry-Perot cavity.

The devices had a single metal contact on the p-side through which current was injected into the entire 500μm length of the Fabry-Perot cavity. A typical device is shown in Figure 2.23. The optical output was fibre-coupled into an optical spectrum analyser. The threshold currents are plotted in Figure 2.24 (a), peak optical power in Figure 2.24 (b) while Figure 2.24 (c) shows the percentage of single-moded (with SMSR > 15dB) optical spectrum for a sweep of the injection current from 0 to 90mA in steps of 2mA.

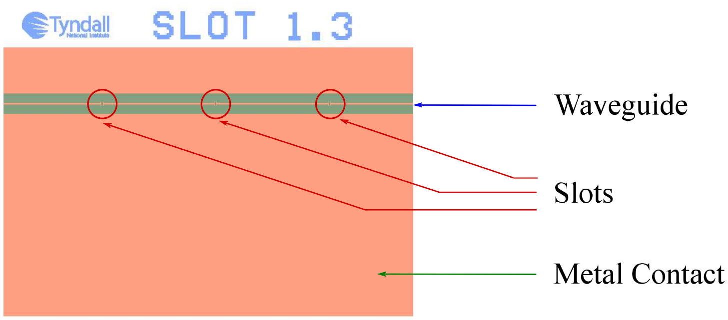

Figure 2.23: Slotted Fabry-Perot laser of length 500μm with two slots equally spaced along the cavity and a single metal contact

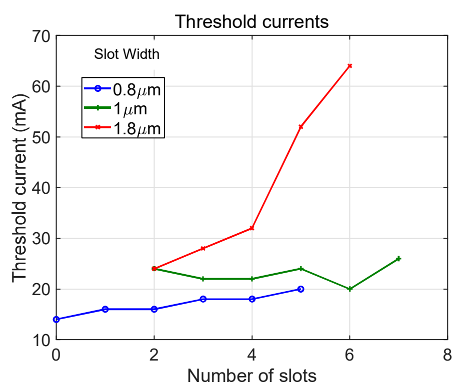

(a)

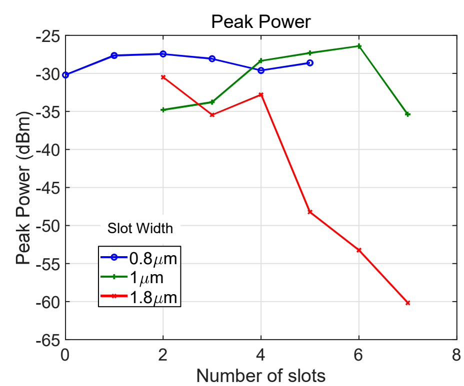

(b)

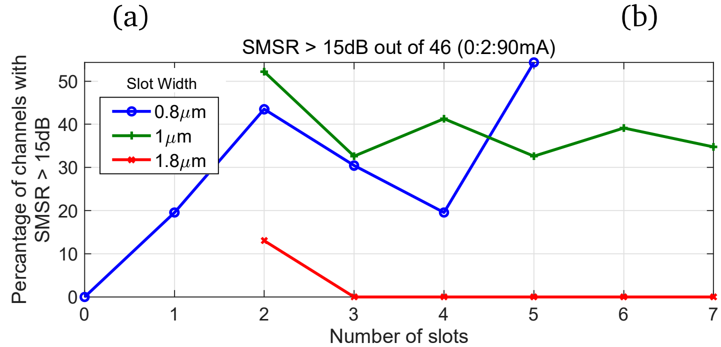

(c)

Figure 2.24: (a) Threshold current (b) Peak optical power (c) Percentage of single-mode lasing as a function of slot width and number of slots

We observe from Figure 2.24 (a) and (b) that a slot width of 1.8μm results in larger threshold currents and poor optical output power, especially as the number of slots increases. And from Figure 2.24 (c), it can be seen that slots with a width of 1.8μm perform very poorly in terms of single-modedness, whereas slots of widths around 1μm lase show better single mode lasing characteristics. From Figure 2.24 (a), (b) and (c), we can infer that slots of width of around 1μm and 2 slots along the length of the Fabry-Perot cavity result in good performance of the device in terms of threshold current, power and single-modedness.

2.4.2 Multi-section slotted Fabry-Perot lasers

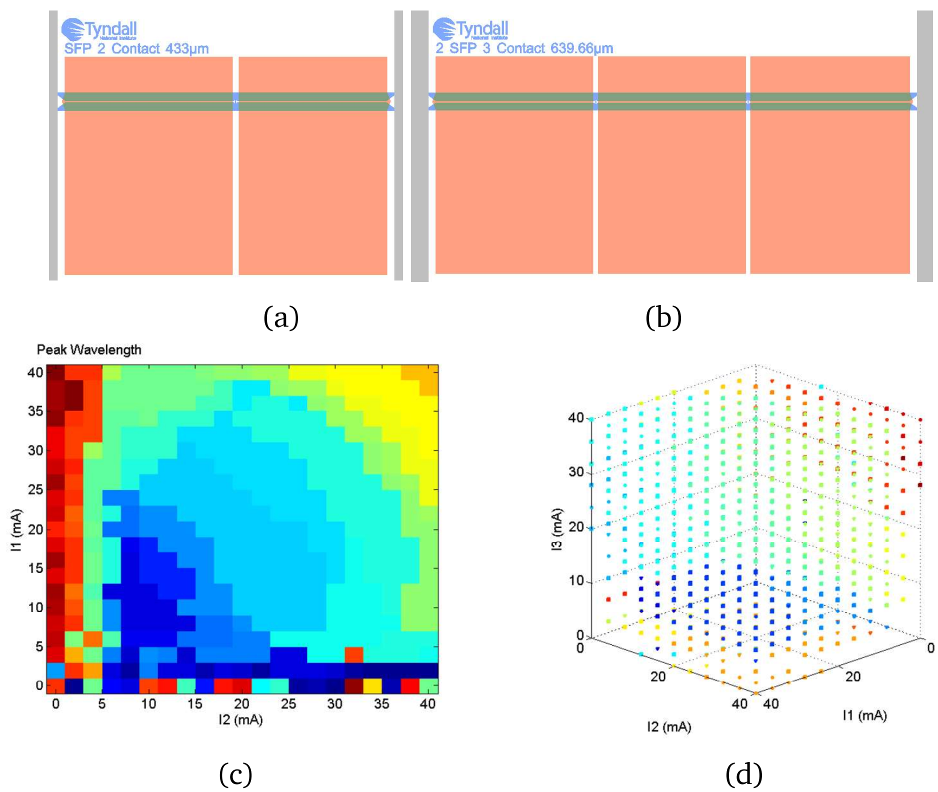

Figure 2.25: Typical (a) 2-section (b) 3-section slotted Fabry-Perot lasers. Tuning map – peak wavelength from (c) 2-section (d) 3-section slotted Fabry-Perot laser

Figure 2.25 (a) shows a typical 2-section slotted Fabry-Perot laser fabricated using this process. The two sections of the Fabry-Perot cavity are separated by one slot and metal contacts on the p-side of the device are also separated so that the two sections can be injected with different currents. The lengths of the two sections are 229μm and 203μm. The lengths are chosen to be different to avoid possibility of resonances from cavities of equal length. Currents were injected into the two sections ranging from 0 to 40mA in each section in steps of 2mA. The output facet was fibre-coupled into an optical spectrum analyser. Figure 2.25 (c) shows the peak wavelength as a function of the two currents. We can observe bands of different peak wavelengths in the plot which tends to shift to longer wavelengths as the total current in the device increases. Figure 2.25 (b) shows a similar device but with 2 slots and hence 3 sections. The lengths of the sections are 215, 195, 217μm. And Figure 2.25 (d) is a 3-dimensional plot that shows the peak wavelength as a function of the three currents in the different sections of the device.

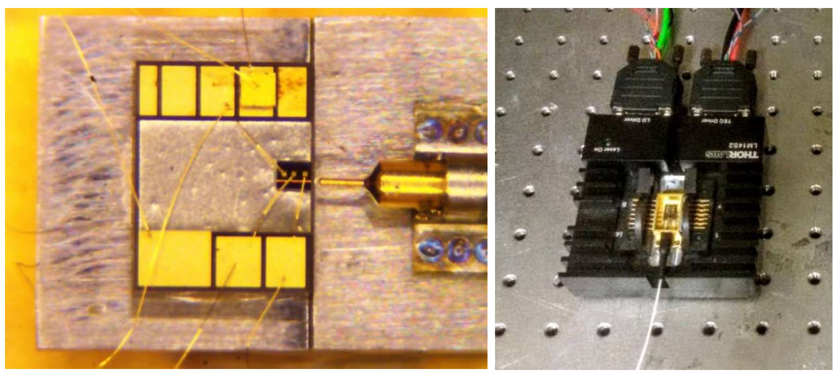

Figure 2.26: Three-section laser in a butterfly package

A 3-section slotted Fabry-Perot device was mounted inside a butterfly package with the help of the Photonics Devices Packaging group in Tyndall National Institute. The laser chip was glued onto an Aluminium Nitride submount containing a thermo-electric cooler (TEC), a lensed-fibre was aligned to its facet and its contact pads were wire-bonded to the arms of the butterfly package. A picture of this package is shown in Figure 2.26. The currents in the three sections of the laser were varied between 0 and 40mA in steps of 2mA. The resultant wavelength channels are shown in Figure 2.27. This is a coarse sweep that shows the range and behavior of a typical device. It should be noted that there are considerable gaps in the tuning maps which can be accessed by a smaller step size in the current sweep which takes considerably longer to obtain. For instance, a sweep between 0 and 40mA with a step size of 2mA for the three currents results in a dataset with 9261 points (21x21x21) which takes about 3.5 hours to run. The bottleneck is the sweep of the OSA which takes about 1.3 seconds. A sweep with a smaller step size of 1mA was executed taking about 28 hours that resulted in a dense channel map as shown in Figure 2.28 (a).

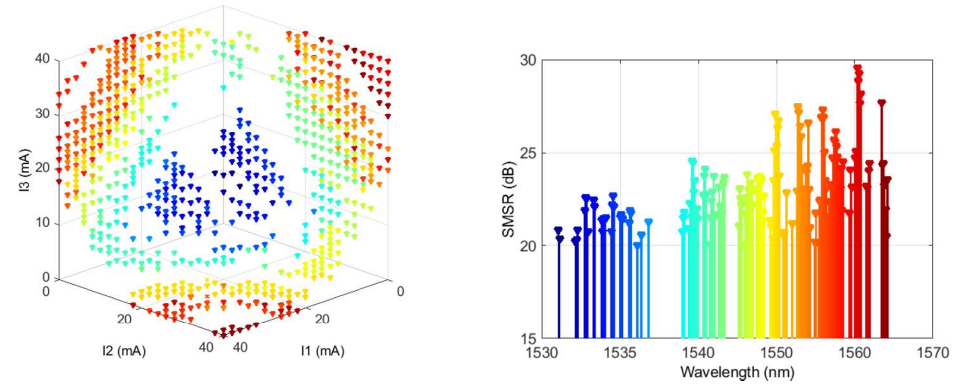

(a) (b)

Figure 2.27: (a) Tuning map – peak wavelength as a function of three section currents and (b) the corresponding wavelength channels and their SMSRs

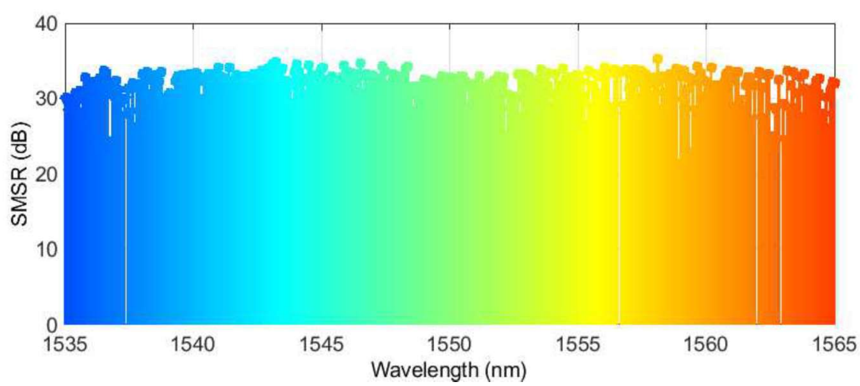

(a)

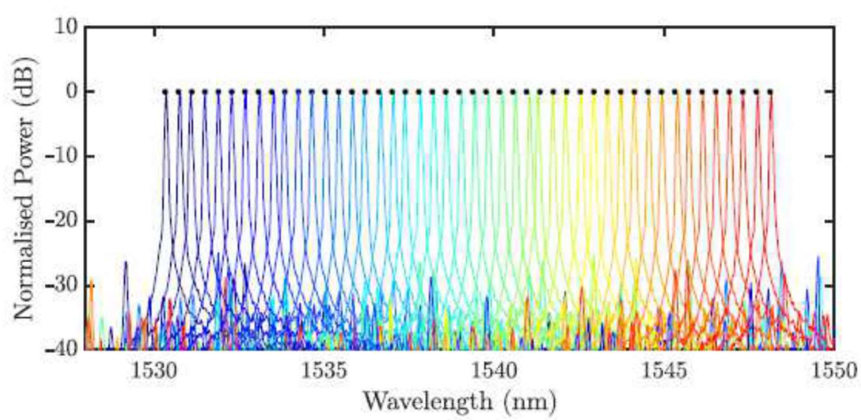

(b)

Figure 2.28: (a) Dense wavelength channels and (b) channels from the ITU-T 50 GHz grid obtained using the 3-section slotted Fabry-Perot laser mounted in the butterfly package

For telecommunication applications, it is useful to have the laser tuned to the standard wavelengths set by the International Telecommunication Union (ITU-T). From the dense channel map in Figure 2.28(a), it is evident that wavelengths close to these channels can be obtained for certain values of current combinations. When tuning the three currents is not enough to exactly hit a wavelength channel in the ITU-T grid, the temperature of the device can be altered by controlling the TEC making this a fine-tuning control knob in addition to the currents. Figure 2.28(b) shows the resultant spectra of the all the channels of the ITU-T 50GHz grid in the lower half of the C-band by using the temperature control between 16C and 22C. The obtained SMSRs for all the channels were near 30 dB making this a good candidate for a tuneable laser in telecommunication applications.

2.5 Summary

Summary goes here

References

[1] L. Coldren, K. Ebeling, B. Miller, and J. Rentschler, "Single longitudinal mode operation of two-section GaInAsP/InP lasers under pulsed excitation," *IEEE Journal of Quantum Electronics*, vol. 19, pp. 1057–1062, June 1983.

[2] B. Corbett and D. McDonald, "Single longitudinal mode ridge waveguide 1.3 μm fabry-perot laser by modal perturbation," *Electronics Letters*, vol. 31, pp. 2181–2182, Dec 1995.

[3] R. N. Hall, G. E. Fenner, J. D. Kingsley, T. J. Soltys, and R. O. Carlson, "Coherent light emission from GaAs junctions," *Phys. Rev. Lett.*, vol. 9, pp. 366–368, Nov 1962.

[4] M. I. Nathan, W. P. Dumke, G. Burns, F. H. D. Jr., and G. Lasher, "Stimulated emission of radiation from GaAs p-n junctions," *Applied Physics Letters*, vol. 1, no. 3, pp. 62–64, 1962.

[5] H. Kroemer, "Zur theorie des diffusions und des drifttransistors; III. dimensionierungsfragen," *Arch. Elektr. Übertrag*, vol. 8, pp. 499–504.

[6] H. Kroemer, "The double-heterostructure concept: How it got started," *Proceedings of the IEEE*, vol. 101, pp. 2183–2187, Oct 2013.

[7] H. Kroemer, "A proposed class of hetero-junction injection lasers," *Proceedings of the IEEE*, vol. 51, pp. 1782–1783, Dec 1963.

[8] Z. I. Alferov and R. F. Kazarinov. Author's certificate no. 1032155/26-25 USSR, 1963.

[9] I. Hayashi, M. B. Panish, P. W. Foy, and S. Sumski, "Junction lasers which operate continuously at room temperature," *Applied Physics Letters*, vol. 17, no. 3, pp. 109–111, 1970.

[10] Z. I. Alferov, V. M. Andreev, D. Z. Garbuzov, Y. V. Zhilyaev, E. P. Mo-

rozov, E. L. Portnoi, and V. G. Trofim, "Investigation of the influence of the AlGaAs-GaAs heterostructure parameters on the laser threshold current and the realization of the continuous emission at the room temperature," *Sov. Phys. Semiconductors*, vol. 4, 1970. Translated from Fiz. Tekh. Poluprovodn. 4.

[11] J. Buus, M. Amann, and D. Blumenthal, *Tunable Laser Diodes and Related Optical Sources*. Wiley, 2005.

[12] T. Higashi, S. J. Sweeney, A. F. Phillips, A. R. Adams, E. P. O'Reilly, T. Uchida, and T. Fujii, "Observation of reduced nonradiative current in 1.3μm AlGaInAs-InP strained mqw lasers," *IEEE Photonics Technology Letters*, vol. 11, pp. 409–411, April 1999.

[13] Y.-K. Kuo, S.-H. Yen, M.-W. Yao, M.-L. Chen, and B.-T. Liou, "Numerical study on gain and optical properties of AlGaInAs, InGaNAs, and InGaAsP material systems for 1.3μm semiconductor lasers," *Optics Communications*, vol. 275, no. 1, pp. 156 – 164, 2007.

[14] D. Botez, "Analytical approximation of the radiation confinement factor for the TE_0 mode of a double heterojunction laser," *IEEE Journal of Quantum Electronics*, vol. 14, pp. 230–232, April 1978.

[15] R. People and J. C. Bean, "Calculation of critical layer thickness versus lattice mismatch for Ge_xSi_{1-x}/Si strained layer heterostructures," *Applied Physics Letters*, vol. 47, no. 3, pp. 322–324, 1985.

[16] P. J. A. Thijs, L. F. Tiemeijer, P. I. Kuindersma, J. J. M. Binsma, and T. V. Dongen, "High-performance 1.5 mu;m wavelength ingaas-ingaasp strained quantum well lasers and amplifiers," *IEEE Journal of Quantum Electronics*, vol. 27, pp. 1426–1439, Jun 1991.

[17] W. T. Tsang, "A graded-index waveguide separate confinement laser with very low threshold and a narrow gaussian beam," *Applied Physics Letters*, vol. 39, no. 2, pp. 134–137, 1981.

[18] W. T. Tsang, N. A. Olsson, R. A. Logan, J. A. Ditzenberger, I. P. Kaminow, and J. Ko, "Single-longitudinal-mode performance characteristics of cleaved-coupled-cavity lasers," *Applied Physics Letters*, vol. 43, no. 11, pp. 1003–1005, 1983.

[19] *Photonic Integrated Circuits*, ch. Eight, pp. 451–507. Wiley-Blackwell, 2012.

[20] S. O'Brien and E. P. O'Reilly, "Theory of improved spectral purity in index patterned fabry-pérot lasers," *Applied Physics Letters*, vol. 86, no. 20, p. 201101, 2005.

[21] P. Lambkin, C. Percival, and B. Corbett, "Reflectivity measurements of intracavity defects in laser diodes," *IEEE Journal of Quantum Electronics*, vol. 40, pp. 10–17, Jan 2004.

[22] Q. Y. Lu, W. H. Guo, R. Phelan, D. Byrne, J. F. Donegan, P. Lambkin, and B. Corbett, "Analysis of slot characteristics in slotted single-mode semiconductor lasers using the 2-d scattering matrix method," *IEEE Photonics Technology Letters*, vol. 18, pp. 2605–2607, Dec 2006.

[23] J. Zhao, K. Shi, Y. Yu, and L. P. Barry, "Theoretical analysis of tunable three-section slotted fabry-perot lasers based on time-domain traveling-wave model," *IEEE Journal of Selected Topics in Quantum Electronics*, vol. 19, pp. 1–8, Sept 2013.

[24] P. Vettiger, M. K. Benedict, G. L. Bona, P. Buchmann, E. C. Cahoon, K. Datwyler, H. P. Dietrich, A. Moser, H. K. Seitz, O. Voegeli, D. J. Webb, and P. Wolf, "Full-wafer technology-a new approach to large-scale laser fabrication and integration," *IEEE Journal of Quantum Electronics*, vol. 27, pp. 1319–1331, Jun 1991.

[25] C.-E. Zah, R. Bhat, B. N. Pathak, F. Favire, W. Lin, M. C. Wang, N. C. Andreadakis, D. M. Hwang, M. A. Koza, T.-P. Lee, Z. Wang, D. Darby, D. Flanders, and J. J. Heieh, "High-performance uncooled 1.3 μm $Al_xGa_yIn_{1-x-y}As$/InP strained-layer quantum-well lasers for subscriber loop applications," *IEEE Journal of Quantum Electronics*, vol. 30, pp. 511–523, Feb 1994.

[26] J. C. L. Yong, J. M. Rorison, R. V. Penty, and I. H. White, "Material gain comparison for InGaAsP, AlGaInAs and InGaAsN for 1.3 micron laser diode," in *Technical Digest. Summaries of papers presented at the Conference on Lasers and Electro-Optics. Postconference Technical Digest (IEEE Cat. No.01CH37170)*, pp. 479–480, May 2001.